

Soret coefficient of the *n*-dodecane–*n*-hexane binary mixture under high pressure^{*}

Ion Lizarraga¹, Fabrizio Croccolo^{2,3}, Henri Bataller², and M. Mounir Bou-Ali^{1,a}

¹ MGEP Mondragon Goi Eskola Politeknikoa, Mechanical and Industrial Manufacturing Department, Loramendi 4, Apartado 23, 20500 Mondragon, Spain

² Univ. Pau & Pays Adour, CNRS, TOTAL, LFCR-IPRA, UMR5150, 1 allée du Parc Montaury, 64600 Anglet, France

³ CNES Centre National d'Études Spatiales, 2 place Maurice Quentin, 75 039 Paris Cedex 01, France

Received 30 September 2016 and Received in final form 4 January 2017

Published online: 31 March 2017 – © EDP Sciences / Società Italiana di Fisica / Springer-Verlag 2017

Abstract. In the present work, the Soret coefficient has been determined at high pressure for a binary hydrocarbon mixture by combining the thermogravitational column and the dynamic near-field imaging techniques. The analyzed mixture is an iso-massic *n*-dodecane–*n*-hexane mixture at 298.15 K. The molecular diffusion coefficient has been measured up to 20 MPa by means of the dynamic analysis of the light scattered by non-equilibrium concentration fluctuations. With a cylindrical thermogravitational column the thermodiffusion coefficient was determined from 0.1 MPa to 10 MPa. Density, as well as, mass expansion and thermal expansion have been measured with a high pressure densimeter. Dynamic viscosity at up to 20 MPa has been determined with a high pressure viscometer. This work shows the decreasing tendency of both the molecular diffusion and the thermodiffusion coefficient with increasing pressure.

1 Introduction

Thermodiffusion, or Soret effect, is a transport phenomenon that couples heat and mass fluxes [1] and can also lead to convective unstable conditions in particular cases [2]. At constant pressure, a temperature gradient in a binary fluid induces thermal diffusion and, thus, a component separation by means of the Soret effect. The segregation induces then Fickian diffusion and the combination of the two phenomena results in a steady concentration gradient, which is convection-free only in microgravity conditions, or in particular cases on ground. Restricting our interest to the binary mixtures, in the framework of (linear) non-equilibrium thermodynamics, one can write the total mass flux of the denser component \vec{j} as

$$\vec{j} = -\rho[D\nabla c + D_T c_0(1 - c_0)\nabla T], \quad (1)$$

where ρ is the fluid density, D the mass diffusion coefficient, ∇c the concentration gradient (of the denser component), D_T the thermodiffusion coefficient, c_0 the mass fraction and ∇T the temperature gradient. This expression gives the value and the direction of the relative separation of the molecules along the temperature gradient.

^{*} Contribution to the Topical Issue “Non-isothermal transport in complex fluids”, edited by Rafael Delgado-Buscalioni, Mohamed Khayet, José María Ortiz de Zárate and Fabrizio Croccolo.

^a e-mail: mbouali@mondragon.edu

At the steady state, the flux vanishes and the resulting ratio of concentration and temperature gradients is often quantified by the so-called Soret coefficient, S_T , namely

$$\nabla c = -S_T c_0(1 - c_0)\nabla T \quad (2)$$

with

$$S_T = \frac{D_T}{D}. \quad (3)$$

A thermodiffusion experiment on ground is typically performed by applying a stabilizing thermal gradient to a multicomponent mixture. Thermodiffusion coefficients can also be measured in convective thermo-gravitational columns.

Thermodiffusion coefficient is an important transport property that has to be well understood from both experimental and theoretical points of view, in particular its dependence on pressure, where scarce research has been done so far. Moreover, thermodiffusion at high pressure (HP) is of relevance in several practical engineering problems, as for instance to describe the vertical distribution of the species in hydrocarbon reservoirs [2–5]. Indeed, in oil wells temperature and pressure increase considerably with depth. These conditions make the Soret coefficient to have strong impact in the species segregation and distribution [4–6]. HP thermodiffusion at pressures near to or above thermodynamic critical point (or *locus*) is also of great significance for combustion research [7,8].

However, the contribution of thermodiffusion is difficult to quantify in these problems, mainly due to a lack of experimental HP data. In the last years, only one work describing the thermodiffusion coefficient at high pressure has been published [9], plus two works describing mass diffusion [10, 11] and one describing the Soret coefficient [11]. Those works were developed independently and the mixtures were different. We conclude that, despite the mentioned works, there is a lack of experimental data on transport properties under reservoir [12] or high pressure combustion [7] conditions.

Our purpose here is to contribute to the experimental database of HP diffusion and thermal diffusion coefficients. By using a HP thermogravitational column we have measured the thermodiffusion coefficient D_T up to 10 MPa. By dynamic near-field imaging in a convection-free HP Soret cell, we have measured the mass diffusion coefficient D up to 20 MPa. By combining these two coefficients (eq. (3)), we have estimated the value of the Soret coefficient as a function of the pressure S_T .

The studied system is the binary *n*-dodecane (nC_{12}) – *n*-hexane (nC_6) mixture at 50% mass fraction and at 298.15 K mean temperature. The choice of the system was driven by having this alkane mixture already well characterized at atmospheric pressure [13], at which it has a strong Soret effect. In addition, we recently presented an investigation similar to the current one for the isomassic *n*-decane–*n*-pentane system [9], and we find convenient to investigate a series of alkane mixtures keeping constant the ratio between the numbers of carbons of the two components, while increasing the molecular mass of the individual species.

There have been many attempts in the literature at theoretically modeling diffusion and thermodiffusion coefficients of hydrocarbon mixtures and their temperature and pressure dependence, a review can be found in the paper by Shukla and Firoozabadi [14] and also in ref. [7], where it is discussed how accurate property information is critical to successful computational fluid dynamics studies. Despite the clear importance of theoretical modeling, the purpose of this paper is just to present the experimental methods and results, we shall not compare with diffusion or thermal diffusion models and we left this issue for future investigations. In addition, the validation of models by experiments requires the use of thermophysical property data that not always is available.

The remainder of this paper is organized as follows: in sect. 2 the thermogravitational and near-field-scattering techniques are briefly described, in sect. 3 the experimental results and discussion are shown, finally conclusions are provided in sect. 4.

2 Experimental techniques

2.1 Thermogravitational column

Thermogravitational column (TGC) was first used by Clusius and Dickel in 1938 to study thermodiffusion in gas

mixtures [15]. This first column was made of two concentric vertical cylinders whose gap was filled with the gas mixture to study while the inner cylinder was heated. In this configuration, the horizontal temperature gradient induced convection and due to the Soret effect, separation of the fluid components. A theory called Furry-Jones-Onsager [16] was developed for isotope separation in a TGC which is nowadays used as a basic equation for thermogravitational measurements of transport properties in multicomponent fluids [17].

The thermogravitational column used in this work has cylindrical configuration and stainless steel concentric tubes compose it. The width of the gap is 1.000 ± 0.005 mm. For the design of the column it is important to consider the validity limits of Furry, Jones and Onsager (FJO) theory [18, 19]. The column is able to work in a range of 0.1–50 MPa and it allows all type of fluids in different phases: liquid and liquefied gases. In this work, we have limited the thermogravitational column to liquid mixtures up to 10 MPa.

The liquid mixture inside the high pressure column is introduced from the bottom part. The insertion of the fluid from the bottom reduces the presence of bubbles in the gap. To introduce the mixture inside the column in ambient conditions, it is required compressed air. The air is free from humidity and any impurity dust in order not to contaminate the fluid. Therefore the air is filtered and dried. The compressed air is the responsible to pushes up the mixture that is inside a beaker in constant velocity. A pressure generator system makes the pressurization of the mixture inside the column. It generates pressure up to 50 MPa. This installation is composed by a pressure intensifier of 120 cm³ fluid storage capacity. The pressurization is given through a hydraulic system with proportional valves that make possible to control the pressure inside the column.

The theory of thermogravitational columns establishes a relation between the steady state of the mixture inside the system and the thermogravitational coefficient [20]:

$$D_T = \frac{g \cdot L_x^4}{504} \frac{\alpha}{c_0(1-c_0)\beta \cdot \mu} \frac{\partial \rho}{\partial z}, \quad (4)$$

where L_x is the dimension of the gap, g the gravitational acceleration, α the thermal expansion coefficient, β mass expansion coefficient, c_0 the mass fraction of the reference component in the initial homogeneous mixture, μ the dynamic viscosity and $\partial \rho / \partial z$ the variation of the density along the height of the column in stationary state.

The time necessary to reach to the stationary state in a thermogravitational column is five times the relaxation time t_r given by the following expression [18]:

$$t_r = \frac{9!(L_z v)^2 D}{(g \pi \alpha \Delta T L_x^3)^2}, \quad (5)$$

where L_z is the vertical size of the column, v is the kinematic viscosity ($v = \mu / \rho$), D the molecular diffusion coefficient and ΔT the applied temperature difference. The applied temperature difference in this work is 10 K. However, at the stationary state the separation is independent

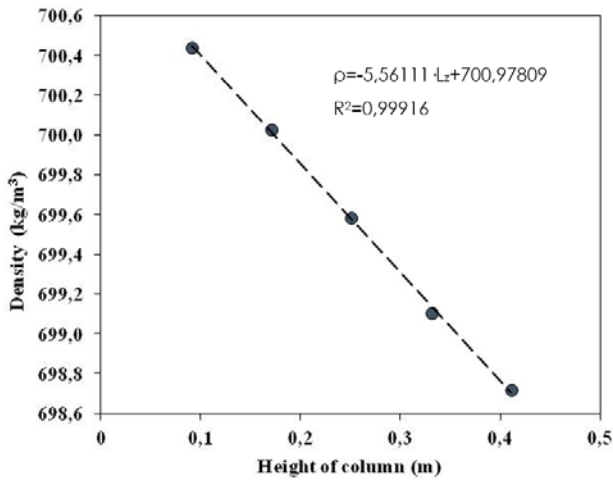


Fig. 1. Density (ρ) variation through the height of the column (L_z) for $nC_{12}-nC_6$ 50 at 298.15 K and 5 MPa at steady state.

of the applied temperature difference. When the relaxation time is over, in the steady state of the mixture, five samples are extracted through the holes that are distributed all of them equidistantly along the height of the column. Measuring each sample in the densimeter, we determine the variation of the density along the height of the column ($\partial\rho/\partial z$) (fig. 1). To make sure that the results are satisfactory, each test is repeated three times. The same procedure is repeated at different pressure conditions: from 0.1 MPa to 10 MPa.

The density, as well as the mass and thermal expansion properties of the mixture are determined by a high pressure (HP) densimeter (Anton Paar, DMA 512P). The system measures up to 70 MPa with a resolution of 10^{-6} g/cm³ and a repeatability of 10^{-5} g/cm³.

The temperature is set by means of an external thermal bath (Lauda, RC6) and monitored by means of a K-type thermocouple with a resolution of 0.1 K. The total internal volume of the HP densimeter is 50 ml of liquid mixture. The HP densimeter functionality is based on the relation between the harmonic vibration period and the mass of the system. The instrument provides a vibration period τ . By the following equation, the density of the fluid at a specific pressure and temperature is determined:

$$\rho(P_i, T_i) = \rho_{ref1}(P_i, T_i) + \frac{\rho_{ref1}(P_i, T_i) - \rho_{ref2}(P_i, T_i)}{\tau_{ref1}^2(P_i, T_i) - \tau_{ref2}^2(P_i, T_i)} \times [\tau^2(P_i, T_i) - \tau_{ref1}^2(P_i, T_i)], \quad (6)$$

where $\rho(P_i, T_i)$ is the density and $\tau(P_i, T_i)$ the vibration period of the analysed mixture at a given pressure and temperature. The precision of the densimeter depends on the reference fluid taken for the calibration. Each mixture under study requires a previous calibration. Depending on the mixture, the reference fluids taken to the calibration changes. The calibration depends on the density range of the study fluid as well as on the study conditions (temperature and pressure) of the mixture. Therefore, as eq. (6) demonstrates, each reference fluid requires previous den-

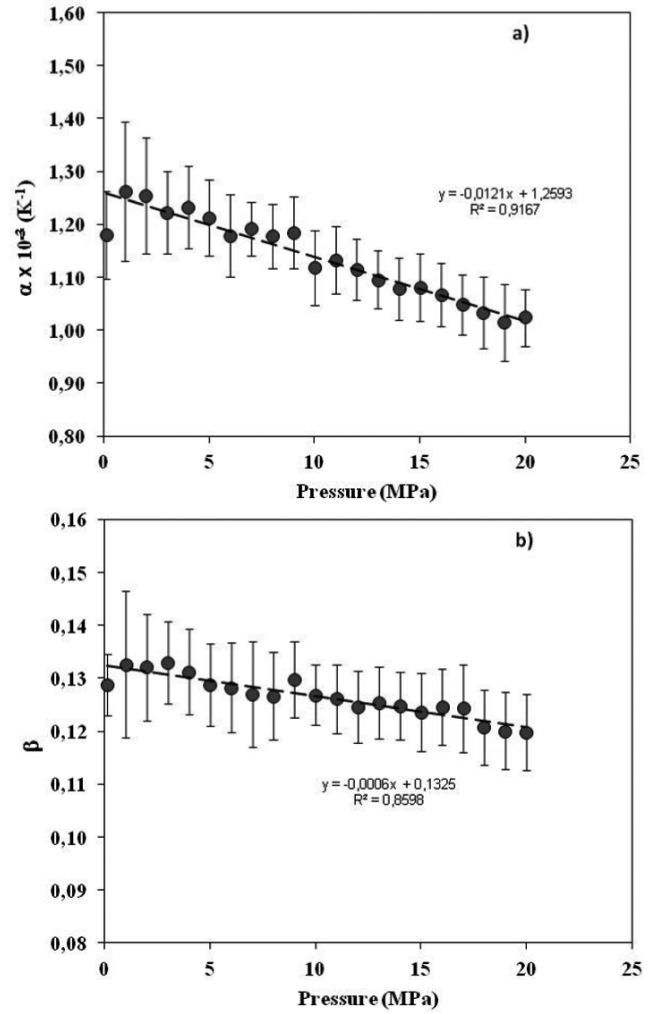


Fig. 2. Mass expansion coefficient (a) thermal expansion coefficient (b) as a function of the pressure for the iso-massic $nC_{12}-nC_6$ binary mixture at 298.15 K.

sity and vibration period values. The density value of the reference fluid at a given pressure and temperature condition are taken from NIST Standard Reference Database 23 (Version 8.0).

The mass fraction of the mixture is always close to the initial mass fraction ($c_0 \pm 0.002$). A linear relationship between the density and the mass fraction is observed in all cases. From the obtained calibration line, we can get the mass expansion coefficient $\beta = (1/\rho)(\partial\rho/\partial c)$. Repeating the density measurements at different temperatures (296.15, 297.15, 298.15, 299.15 and 300.15 K), we determined the thermal expansion coefficient $\alpha = -(1/\rho)(\partial\rho/\partial T)$. Similarly, we calculate α from the calibration relation.

In fig. 2, mass expansion and thermal expansion coefficients are plotted as a function of pressure. Both figures show a linear decreasing tendency of α and β as a function of the pressure.

Dynamic viscosity (μ) has been determined by a commercial HP viscometer (VISCOlab PVT). The device is

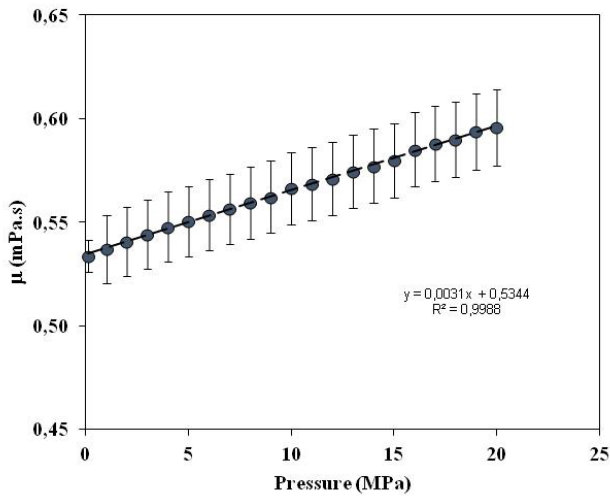


Fig. 3. Dynamic viscosity behaviour as a function of the pressure for the iso-massic nC_{12} - nC_6 binary mixture at 298.15 K.

based on Stokes' law, in which a piston goes up and down due to magnetic forces induced by two magnetized coils inside a stainless steel body. At the same time, the device takes the timing of each stroke determining μ . The viscosity varies considerably with the temperature; hence the temperature needs to be precisely controlled. Therefore, each experimental test is repeated five times for each mixture and the experimental data is stored and processed by VISCOLab PVT Software.

In HP densimeter and viscometer devices, the temperature is controlled by external baths. Thus, the room temperature alters the system temperature resulting in measurement errors larger than those for the corresponding atmospheric devices, which regulate the temperature by Peltier elements. As a further check, we therefore first analyze the mixture at atmospheric pressure in order to compare the obtained value with literature data and eventually perform HP measurements on the same samples.

In fig. 3 we plot the dynamic viscosity as a function of the pressure. It demonstrates that this property increases linearly with the pressure.

2.2 Dynamic near-field imaging

Whenever a temperature gradient is applied to a fluid mixture thermal and concentration non-equilibrium (NE) fluctuations appear. Theory and experiments have shown that NE fluctuations are long-ranged or non-local. These fluctuations are visible at first sight [21]. Moreover, even if their intensity scales as a power-law recently it has been shown that the fronts of diffusion are not fractal [22]. NE fluctuations are strictly related to the transport properties of the fluid. For this reason NE fluctuations analysis can allow determining transport coefficients like viscosity, thermal diffusivity and mass diffusion as well as thermodiffusion coefficients [10, 11, 23, 24]. Ortiz de Zárate and

Sengers book [21] describes elegantly NE fluctuations theory. Temperature and concentration fluctuations result in refractive index fluctuations in the fluid, which are responsible for the light scattered by the sample [25]. Near-field imaging is a family of optical techniques [26–31] in which the light scattered by an illuminated sample is collected by a pixilated detector together with the (much more intense) transmitted beam in the near field, *i.e.* sufficiently close to the sample to overlap on the detector providing interference. In this way, the refractive index fluctuations that are not visible at the sample plane, are transformed into detectable intensity fluctuations and can be recorded in the form of series of images. The main difference of Near-Field Scattering [26, 27], Shadowgraph [32, 33] and Schlieren [33, 34] techniques is the \vec{q} wave vector range. In our experimental procedure, a series of such image maps are statistically analyzed by Fourier transform. As stated, spatial and temporal fluctuations of the refractive index inside the sample are related to its temperature and concentration fluctuations. Here we apply the Differential Dynamic Algorithm [10, 11, 23, 24, 30, 35–40], in order to extract the temporal correlation function of NE fluctuations.

Details of the quantitative dynamic analysis can be found elsewhere [28, 35, 36, 41, 42]. We simply recall that the result of the image analysis is the experimental structure function obtained by averaging over all available times contained in each image dataset and over all the wave vectors with equal modulus. In fig. 4, a sample image, an image difference and a 2D-spatial Fourier transform of the difference image are shown.

The obtained experimental structure function is theoretically related to the temporal correlation function of NE fluctuations, also called intermediate scattering function (*ISF*), by

$$C_m(q, t) = 2 \{S(q)T(q)[1 - ISF(q, \Delta t)] + B(q)\} \quad (7)$$

with $ISF(q, 0) = 1$. $S(q)$ is the static power spectrum of the sample, $T(q)$ the optical transfer function and $B(q)$ the background noise of the measurement. In eq. (7) the linear response of the CCD detector and any other electronic or electromagnetic proportionality parameters are implicitly included into $T(q)$ and/or $B(q)$.

In a binary mixture, the temporal correlation function of NE concentration fluctuations induced by the Soret effect is expected to be a single exponential decay for all wave vectors, with time constants $\tau_S(q)$ varying as a function of the wave vector q . For wave vectors much larger than a characteristic value q_s^* , the decay time is the solutal diffusive one:

$$\tau_S(q) = 1/(Dq^2) \quad (8)$$

NE thermal fluctuations are faster and overlap to the solutal ones. For wave vectors larger than a thermal characteristic wave vector q_T^* , the decay time is the thermal diffusive one:

$$\tau_T(q) = 1/(\kappa q^2), \quad (9)$$

where κ is the thermal diffusivity coefficient.

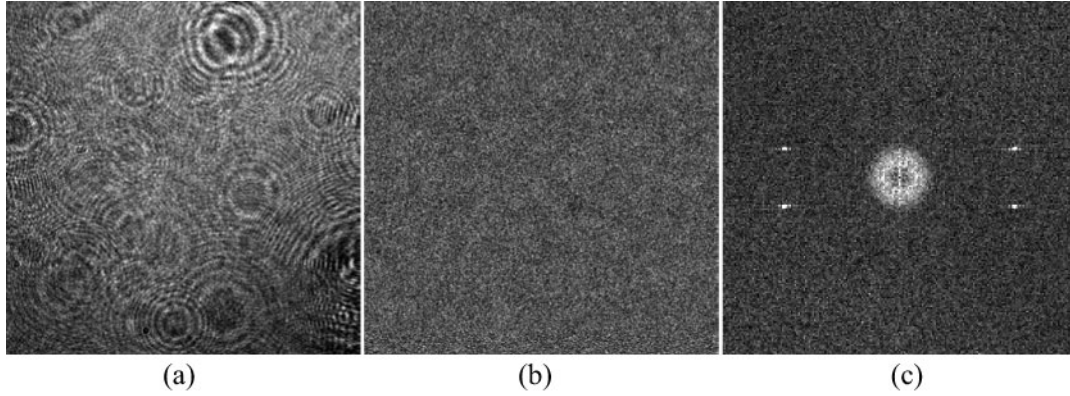


Fig. 4. Results of a near-field scattering experiment (shadowgraph layout) on the iso-massic binary n -dodecane– n -hexane mixture stressed by a thermal gradient ($T_{\text{mean}} = 323.15$ K, $P = 20$ MPa, $\Delta T = 30$ K): (a) 768×768 pixel near-field image of the sample, $I(\vec{x}, t)$; (b) image difference, $\Delta I(\vec{x}, \Delta t) = I(\vec{x}, t + \Delta t) - I(\vec{x}, t)$, having a correlation time of $\Delta t = 0.35$ s and; (c) 2D Fast Fourier Transform squared $\Delta I(\vec{x}, \Delta T) = I(\vec{x}, t + \Delta T) - I(\vec{x}, t)$ of (b).

Table 1. Density ρ , thermal α and mass β expansion coefficients, dynamic viscosity μ and density vertical gradient values in the thermogravitational column for nC_{12} - nC_6 50 wt.% at 298.15 K as a function of the pressure.

Pressure (MPa)	ρ (kg/m ³)	$\alpha \times 10^{-3}$ (K ⁻¹)	β	μ (mPa s)	$\delta\rho/\delta z$ (kg/m ⁴)
0.1	699.037	1.180 ± 0.083	0.129 ± 0.006	0.534 ± 0.008	5.973 ± 0.131
2	700.959	1.25 ± 0.078	0.132 ± 0.008	0.540 ± 0.017	5.689 ± 0.058
4	702.737	1.213 ± 0.072	0.131 ± 0.008	0.547 ± 0.017	5.549 ± 0.053
6	704.562	1.179 ± 0.069	0.128 ± 0.009	0.553 ± 0.017	5.416 ± 0.069
8	706.198	1.178 ± 0.051	0.126 ± 0.010	0.559 ± 0.017	5.219 ± 0.081
10	707.908	1.118 ± 0.070	0.127 ± 0.006	0.566 ± 0.017	5.117 ± 0.068

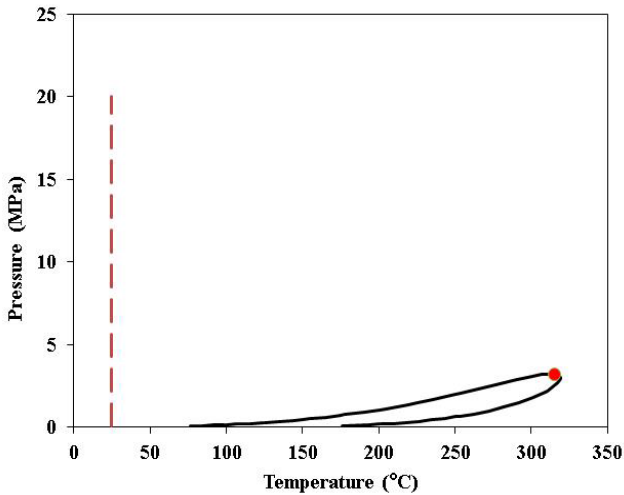


Fig. 5. Phase diagram of the isomassic nC_{12} - nC_6 binary mixture. The 298.15 K mean temperature and the pressure range used in the experiments is indicated.

3 Experimental results and discussion

The overall objective of this study is to determine the transport properties of the iso-massic nC_{12} - nC_6 binary mixture at high pressure and 298.15 K by combining the

thermogravitational column and the dynamic near-field imaging techniques.

3.1 Thermodynamic conditions

By means of TOTAL S.A. company BEST software, we have determined the thermodynamic conditions for the investigated mixture in order to ensure that we are working in a monophasic area (fig. 5). The phase diagram for hydrocarbon mixtures is based on the modified Peng-Robinson equation of state (EoS) PPR78 [42,43]. This EoS is widely used in the field of petroleum engineering to predict fluid in equilibrium properties [44]. In fig. 5 we can appreciate monophasic and biphasic ranges. The X-axis represents the temperature and the Y-axis represents the pressure. The vertical line represents the conditions of our experiments. In all the investigation conditions (temperature of 298.15 K and pressures from atmospheric up to 20 MPa) the mixture is in the liquid state.

3.2 Thermodiffusion coefficient

For the determination of the thermodiffusion coefficient, according to eq. (4), it is necessary to know the required thermophysical properties at the desired temperature and pressure conditions. Table 1 shows data for density, thermal and mass expansion coefficients and dynamic viscosity at different pressure conditions. Values of the variation

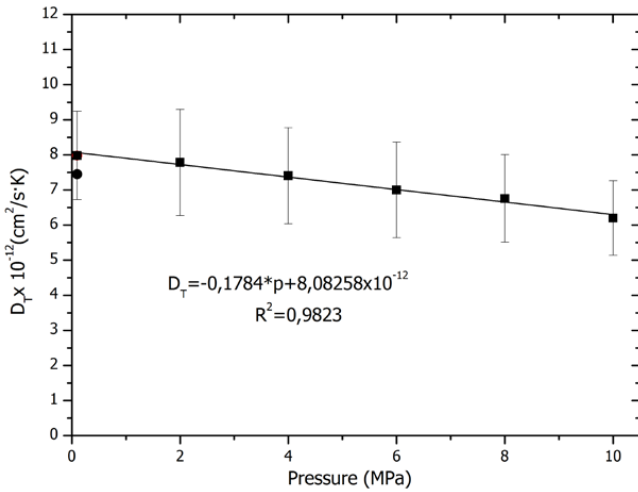


Fig. 6. Thermodiffusion coefficient *versus* pressure for nC_{12} - nC_6 50 wt.% at 298.15 K. ■: high pressure measurements; ●: reference value from Alonso de Mezquía *et al.* [13].

of the density along the height of the column ($\partial\rho/\partial z$) in steady state are also presented up to 10 MPa.

In fig. 6 we report the values of the thermodiffusion coefficient D_T as a function of the pressure. We can notice a slight linear decrease with pressure, similar to the behavior obtained for the binary mixtures of n -dodecane, isobutylbenzene and 1,2,3,4 tetrahydronaphthalene by Urteaga *et al.* [9]. In comparison with the mentioned work, we can note that the pressure effect is larger for mixtures of alkanes.

The black spot at 0.1 MPa represents the atmospheric value from Alonso de Mezquía *et al.* [13]. This variance between both values is due to the fact that in the HP densimeter and HP viscometer, the temperature control is not totally steady. The inaccuracy of the temperature comes from the tempering of the external thermostatic bath as well as from the variation of the temperature of the room. The density value from the reference pure fluids required for the calibration of the HP densimeter is another factor that alters the value of D_T .

3.3 Mass diffusion coefficient and thermal diffusivity

For the measurement of the mass diffusion coefficient we made use of the same HP thermodiffusion cell with a shadowgraph setup as in previous experiments [10,11]. Experiments have been performed with the iso-massic binary mixture of n -dodecane and n -hexane. The average temperature of the sample is set to 298.15 K, so that the system is liquid at any pressure utilized in the present study, from atmospheric to HP.

We perform a series of shadowgraph experiments, by imposing a vertical temperature difference $\Delta T = 20$ K to the horizontal fluid layer with a RMS stability of about 1 mK over 24 h. The thickness of the fluid inside the cell is $L = 5$ mm. The vertical temperature gradient is applied via two distinct controllers, so that a linear temperature

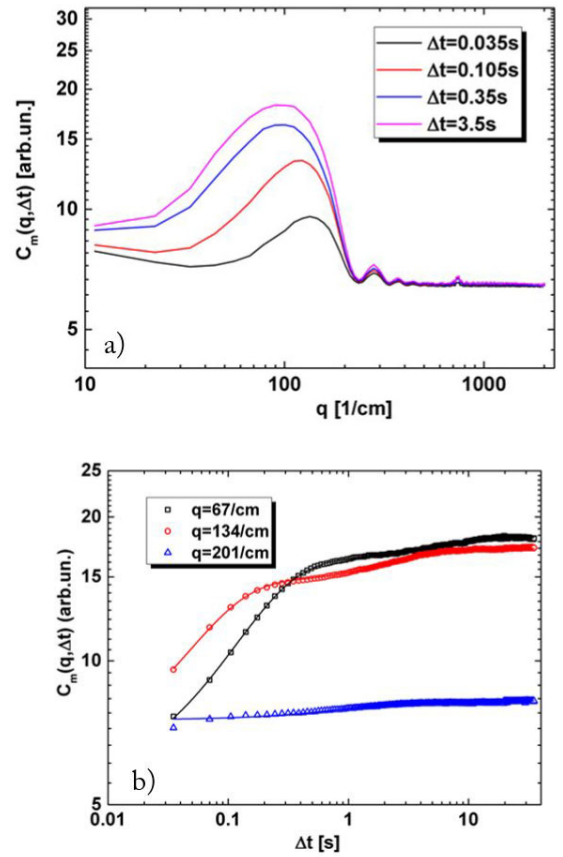


Fig. 7. Experimental structure function $C_m(q, \Delta t)$ (a) as a function of wave vector (q) for different correlation times (Δt); and (b) as a function of the correlation time (Δt) for different wave vectors (q) ($T_{\text{mean}} = 298.15$ K, $P = 10$ MPa, $\Delta T = 20$ K).

gradient sets up in some tens of seconds. The image acquisition starts about five hours later, to ensure that the concentration gradient generated by the Soret effect is fully developed in the cell, a sufficiently large time compared to a vertical diffusion time across the layer thickness L of $\tau_d = L^2/\pi^2 D \approx 1200$ s, is calculated with the reference value of the diffusion coefficient at atmospheric pressure [42]. The pressure is changed from the atmospheric up to 20 MPa.

The detection plane is located at about $z = 95$ mm from the sample plane. As a sensor, we use a charge coupled device (AVT, PIKE-F421B) with 2048×2048 square pixels each of size $7.4 \times 7.4 \mu m^2$ and a dynamic range of 14-bit. Images were cropped within a 768×768 pix² area in order to reach the maximum acquisition frame rate of the camera of about 30 Hz.

At each investigated pressure P , 10 different image acquisition runs have been performed with a delay time $dt_{\text{min}} = 35$ ms between two consecutive images. Each set, containing 2000 images, has then been processed on a dedicated PC by means of a custom-made CUDA/C++ software [41], in order to perform a fast parallel processing of the images to obtain the structure functions $C_m(q, \Delta t)$, for all the wave numbers and for all the correlation times accessible within the image datasets.

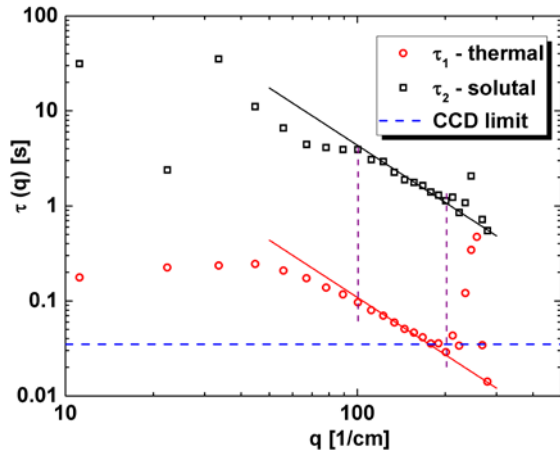


Fig. 8. Experimental decay times of NE fluctuations as obtained by fitting the structure function through eqs. (7) and (10), as a function of the wave number q . \circ : fast mode, \square : slow mode ($T_{\text{mean}} = 298.15$ K, $P = 10$ MPa, $\Delta T = 20$ K). The black solid line represents the theoretical relaxation times $1/Dq^2$ of eq. (8) and the red solid line represents the theoretical relaxation times $1/\kappa q^2$ of eq. (9).

Experimental structure functions are shown in fig. 7, both as a function of the wave number (q) and the correlation time (Δt). They are further analyzed by fitting for each q as a function of the Δt by means of eq. (7) with an *ISF* including the two exponentials described by eqs. (8), (9). The *ISF* thus can be described as

$$ISF(q, \Delta t) = a \cdot e^{-\frac{\Delta t}{\tau_1(q)}} + (1 - a)e^{-\frac{\Delta t}{\tau_2(q)}}. \quad (10)$$

From this procedure, two decay times can be extracted for all the wave numbers. It is clearly visible from fig. 8 that the two decay times are well separated by a factor of about ten over the wave number range. The fastest mode is then attributed to the temperature fluctuations, while the slowest one to concentration fluctuations. For wave numbers larger than a given value (different for thermal and solutal modes), the time decay displays a power-law behavior compatible with eqs. (8), (9), *i.e.* they show diffusive behavior. Further fitting time decay data with eqs. (8), (9) thus provides the values of the thermal diffusivity and of mass diffusion coefficient for the temperature and concentration fluctuations, respectively. The fitting lines obtained at $P = 10$ MPa are shown in fig. 8, too.

Measured values of thermal diffusivity and mass diffusion coefficient are reported in fig. 9 as a function of the pressure. Uncertainties are the average of the deviation with respect to the mean value of the 10 measurements. Thermal diffusivity displays a slight increase as a function of the pressure. Data points are somewhat scattered and a discrepancy of 10% is visible from the reference NIST data within the entire pressure range. Conversely, the mass diffusion coefficient shows a slight linear decrease as a function of the pressure. Data points are less scattered due to the fact that the concentration time decays are larger and thus more reliably captured by the optical setup. We

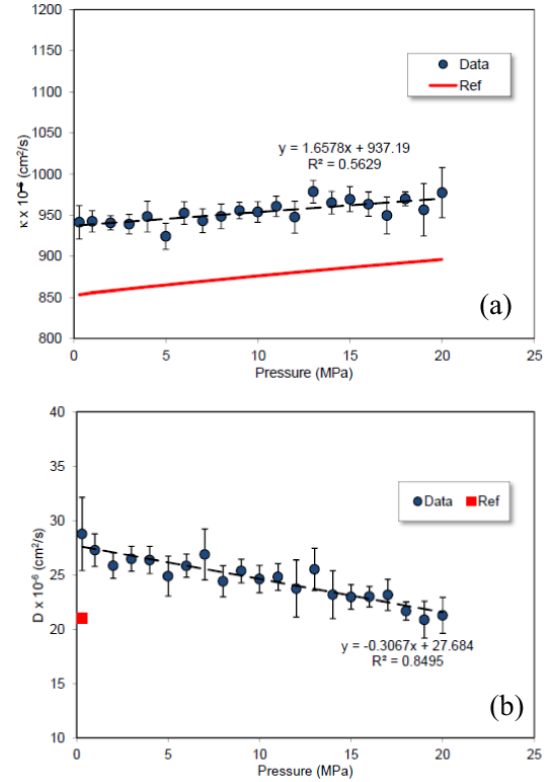


Fig. 9. Values of the (a) thermal diffusivity and (b) mass diffusion coefficient as a function of the pressure. Reference values are reported as (a) red line from NIST database and (b) red point from ref. [13].

remind here that one of the limits of our technique is the frame rate of the CCD camera (here about 30 Hz) that sets the minimum time decay that can be extracted. Data in fig. 9(b) are complemented with a reference value obtained at atmospheric pressure by Alonso de Mezquía *et al.* [13]. We note a discrepancy of about 20%, between our measurement and the reference point, as already observed in a previous study [10]. Given the small amplitude of the structure function for the *n*-dodecane/*n*-hexane mixture (appreciable at low and intermediate wave vectors in fig. 7(a), where the maximum *S/N* ratio is about 5). The poor signal is mainly due to a small value of the optical contrast factor of the mixture combined with a small Soret coefficient [26–30].

3.4 Soret coefficient

As a last point, we have determined the Soret coefficient by using eq. (3) as presented in the first section. In table 2, we report experimental S_T results at different pressures. The calculated values of S_T are determined using the values of D_T and D included in the table at each pressure condition.

The calculated values of the Soret coefficient show a relative error larger than 50%. Given the large uncertainty it is not possible to evidence any pressure effect on the Soret coefficient. However, this is not unexpected since

Table 2. Thermodiffusion, molecular diffusion, thermal diffusivity and Soret coefficients values for the binary mixture formed by nC_{12} - nC_6 50 wt.% at 298.15 K up to 10 MPa.

Pressure (MPa)	$D_T \times 10^{-12}$ (m ² /sK)	$D \times 10^{-9}$ (m ² /s)	$\kappa \times 10^{-8}$ (m ² /s)	$S_T \times 10^{-3}$ (K ⁻¹)
0.1	7.98 ± 1.26	2.90 ± 0.30	–	2.78 ± 0.53
1	–	2.72 ± 0.15	9.43 ± 0.91	–
2	7.78 ± 1.51	2.59 ± 0.12	9.41 ± 0.86	3.01 ± 0.62
3	–	2.64 ± 0.12	9.39 ± 0.94	–
4	7.41 ± 1.37	2.63 ± 0.13	9.48 ± 0.63	2.81 ± 0.55
5	–	2.50 ± 0.20	9.24 ± 0.94	–
6	7.00 ± 1.36	2.58 ± 0.10	9.52 ± 0.80	2.71 ± 0.56
7	–	2.60 ± 0.20	9.43 ± 0.84	–
8	6.76 ± 1.25	2.44 ± 0.14	9.48 ± 0.89	2.77 ± 0.56
9	–	2.53 ± 0.11	9.56 ± 0.85	–
10	6.20 ± 1.06	2.46 ± 0.13	9.54 ± 0.90	2.52 ± 0.46

the thermodynamic conditions investigated in this paper are far from critical conditions as can be seen in fig. 5.

4 Conclusion

In this work, we have experimentally determined the transport properties of a binary alkane mixture at high pressure through a combination between near-field imaging and thermogravimetric column. The analysed mixture is n -dodecane (nC_{12})– n -hexane (nC_6) at 50% mass fraction and 298.15 K mean temperature. We have determined thermophysical properties such as density, mass expansion, thermal expansion and dynamic viscosity. At the same time, the cylindrical configuration column establishes the thermodiffusion coefficient at high pressure: from 0.1 MPa to 10 MPa. In turn, the thermal diffusivity and the molecular diffusion coefficient up to 20 MPa have been determined by the dynamic analysis of the light scattered by concentration and temperature non-equilibrium fluctuations. Both D and D_T decrease linearly with the increment of the pressure. As a result, the Soret coefficient (S_T) is determined at high pressure combining the thermogravimetric column and the dynamic near-field imaging.

This work is supported by the Research Groups (IT1009-16) and MICRO4FAB from the Basque government, TERDISOMEZ (FIS2014-58950-C2-1-P) of the MINECO, DCMIX (AO-2009-0858/1056) and SCCO from the European Space Agency. FC acknowledges support from the Centre National d'Etudes Spatiales (CNES).

Author contribution statement

Ion Lizarraga (PhD Student), Fabrizio Croccolo (Doctor), Henri Bataller (Doctor) and M. Mounir Bou-Ali (Professor) authors have equally participated to the redaction of the manuscript.

References

1. D. de Groot, P. Mazur, *Non-Equilibrium Thermodynamics* (Dover Publications, 1984).
2. G. Galliero, F. Montel, *Understanding compositional grading in petroleum reservoirs thanks to molecular simulations*, in *2009 SPE EUROPEC/EAGE Annual Conference and Exhibition, Amsterdam, 2009*, SPE 121902 paper (Society of Petroleum Engineers, 2009) DOI: 10.2118/121902-MS.
3. C. Lira-Galeana, A. Firoozabadi, J.M. Prausnitz, *Fluid Phase Equilib.* **102**, 143 (1994).
4. L. Høier, C.H. Whitson, *SPE Reserv. Eval. Eng.* **4**, 36 (2001).
5. F. Montel, J. Bickert, A. Lagisquet, G. Galliero, *J. Pet. Sci. Eng.* **58**, 391 (2007).
6. Y. Yusako, I. Tsuneeo, *Numerical investigation of pressure transient responses of a well penetrating a deep geothermal reservoir at super-critical conditions*, in *Twenty-Firts Whorshop on Geothermal Reservoir Engineering* (Stanford University, 1996) pp. 107–112.
7. S. Palle, R.S. Miller, *Combust. Flame* **151**, 581 (2007).
8. K.G. Harstad, J. Bellan, *J. Chem. Phys.* **120**, 5664 (2004).
9. P. Urteaga, M.M. Bou-Ali, D. Alonso De Mezquia, J. Santamaría, C. Santamaría, J.A. Madariaga, H. Bataller, *Rev. Sci. Instrum.* **83**, 074903 (2012).
10. I. Lizarraga, C. Giraudet, F. Croccolo, M.M. Bou-Ali, H. Bataller, *Micrograv. Sci. Technol.* **28**, 545 (2016).
11. C. Giraudet, H. Bataller, F. Croccolo, *Eur. Phys. J. E* **37**, 107 (2014).
12. W.M. Rutherford, J.G. Roof, *J. Phys. Chem.* **53**, 12506 (1959).
13. D. Alonso de Mezquia, Z. Wang, E. Lapeira, M. Klein, S. Wiegand, M.M. Bou-Ali, *Eur. Phys. J. E* **37**, 106 (2014).
14. K. Shukla, A. Firoozabadi, *Ind. Eng. Chem. Res.* **37**, 3331 (1998).
15. K. Clusius, G. Dickel, *Naturwissenschaften* **26**, 546 (1938).
16. W.H. Furry, R.C. Jones, L. Onsager, *Phys. Rev.* **55**, 1083 (1939).
17. J. Valencia, M.M. Bou-Ali, O. Ecenarro, J.A. Madariaga, C.M. Santamaría, *Therm. Nonequilib. Phenom. Fluid Mix.* **584**, 233 (2002).
18. J.J. Valencia, M.M. Bou-Ali, J.K. Platten, O. Ecenarro, J.M. Madariaga, C.M. Santamaría, *J. Non-Equilib. Thermodyn.* **32**, 299 (2007).
19. J.A. Madariaga, C. Santamaría, H. Barrutia, M.M. Bou-Ali, O. Ecenarro, J.J. Valencia, *C.R. Mec.* **339**, 292 (2011).
20. M.M. Bou-Ali, O. Ecenarro, J.A. Madariaga, C.M. Santamaría, J.J. Valencia, *J. Phys.: Condens. Matter* **10**, 3321 (1999).
21. J.M. Ortiz de Zárate, J.V. Sengers, *Hydrodynamic Fluctuations in Fluids and Fluid Mixtures* (Elsevier, Amsterdam, 2006).
22. D. Brogioli, F. Croccolo, A. Vailati, *Phys. Rev. E* **94**, 022142 (2016).
23. F. Croccolo, H. Bataller, F. Scheffold, *J. Chem. Phys.* **137**, 234202 (2012).
24. F. Croccolo, F. Scheffold, H. Bataller, *C.R. Mec.* **341**, 378 (2013).
25. B.J. Berne, R. Pecora, *Dynamic Light Scattering: With Applications to Chemistry, Biology, and Physics* (Dover Publications, 2000).

26. M. Giglio, M. Carpineti, A. Vailati, Phys. Rev. **85**, 1416 (2000).
27. F. Ferri, D. Magatti, D. Pescini, M.A. Potenza, M. Giglio, Phys. Rev. E **70**, 41405 (2004).
28. F. Croccolo, D. Brogioli, A. Vailati, M. Giglio, D.S. Cannell, Appl. Opt. **45**, 2166 (2006).
29. F. Scheffold, R. Cerbino, Curr. Opin. Colloid Interface Sci. **12**, 50 (2007).
30. A. Cerbino, R. Vailati, Curr. Opin. Colloid Interface Sci. **14**, 416 (2009).
31. F. Giavazzi, R. Cerbino, J. Opt. **16**, 83001 (2014).
32. S.P. Trainoff, D.S. Cannell, Phys. Fluids **14**, 1340 (2002).
33. D. Croccolo, F. Brogioli, Appl. Opt. **50**, 3419 (2011).
34. D. Brogioli, A. Vailati, M. Giglio, Europhys. Lett. **63**, 220 (2003).
35. F. Croccolo, D. Brogioli, A. Vailati, M. Giglio, D.S. Cannell, Phys. Rev. E **76**, 41112 (2007).
36. F. Croccolo, D. Brogioli, A. Vailati, M. Giglio, D.S. Cannell, Ann. N.Y. Acad. Sci. **1077**, 365 (2006).
37. R. Cerbino, V. Trappe, Phys. Rev. Lett. **100**, 188102 (2008).
38. F. Giavazzi, D. Brogioli, V. Trappe, T. Bellini, R. Cerbino, Phys. Rev. E **80**, 031403 (2009).
39. A. Oprisan, A.L. Payne, Opt. Commun. **290**, 100 (2013).
40. A. Oprisan, S. Oprisan, A. Teklu, Appl. Opt. **49**, 86 (2010).
41. G. Cerchiari, F. Croccolo, F. Cardinaux, F. Scheffold, Rev. Sci. Instrum. **83**, 106101 (2012).
42. F. Croccolo, C. Giraudet, H. Bataller, R. Cerbino, A. Vailati, Micrograv. Sci. Technol. **28**, 467 (2016).
43. D.-Y. Peng, D.B. Robinson, Ind. Eng. Chem. Fundam. **15**, 59 (1976).
44. J.-N. Jaubert, R. Privat, F. Mutelet, AIChE J. **56**, 3225 (2010).